

Numerical investigation of free oblique detonation wave induced by non-intrusive energy deposition

Cite as: AIP Advances **11**, 125119 (2021); <https://doi.org/10.1063/5.0073035>

Submitted: 27 September 2021 • Accepted: 23 November 2021 • Published Online: 15 December 2021

 Wenshuo Zhang (张文硕),  Zijian Zhang (张子健),  Zonglin Jiang (姜宗林), et al.

COLLECTIONS

Paper published as part of the special topic on [Fluids and Plasmas](#)



View Online



Export Citation



CrossMark

ARTICLES YOU MAY BE INTERESTED IN

[Numerical study of detonation wave propagation modes in annular channels](#)

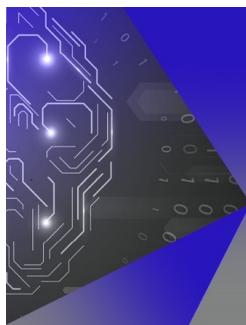
AIP Advances **11**, 085203 (2021); <https://doi.org/10.1063/5.0057586>

[Near-field relaxation subsequent to the onset of oblique detonations with a two-step kinetic model](#)

Physics of Fluids **33**, 096106 (2021); <https://doi.org/10.1063/5.0059439>

[Numerical study of oblique detonation wave initiation in a stoichiometric hydrogen-air mixture](#)

Physics of Fluids **27**, 096101 (2015); <https://doi.org/10.1063/1.4930986>



AIP Machine Learning

Machine Learning for Applied Physics
Applied Physics for Machine Learning

First Articles Now Online!

Numerical investigation of free oblique detonation wave induced by non-intrusive energy deposition

Cite as: AIP Advances 11, 125119 (2021); doi: 10.1063/5.0073035

Submitted: 27 September 2021 • Accepted: 23 November 2021 •

Published Online: 15 December 2021



Wenshuo Zhang (张文硕),^{1,2} Zijian Zhang (张子健),³ Zonglin Jiang (姜宗林),^{1,2} Xin Han (韩信),^{1,2}
Yunfeng Liu (刘云峰),^{1,2,a)} and Chun Wang (王春)^{1,2}

AFFILIATIONS

¹ School of Engineering Science, University of Chinese Academy of Sciences, Beijing 100049, China

² Institute of Mechanics, Chinese Academy of Sciences, Beijing 100190, China

³ Department of Aeronautical and Aviation Engineering, The Hong Kong Polytechnic University, Kowloon, Hong Kong, China

^{a)} Author to whom correspondence should be addressed: liuyunfeng@imech.ac.cn. Fax: +86 10 82543996.

ABSTRACT

To validate the concept of free oblique detonation waves (ODWs) induced by non-intrusive energy deposition applied in ODW engines (ODWEs), numerical simulations are performed by modeling the laser spark as a high-temperature and high-pressure zone embedding in the high-speed incoming flow and by solving the non-dimensional reactive Euler equations with one-step chemistry. The initiation process, flow structures, and self-adapted characteristics of such kinds of free ODWs in an open space are discussed with varying dimensionless source energy and inflow Mach number. The results show that free ODWs can be initiated successfully by local non-intrusive energy deposition. In particular, four ignition regimes, namely, the subcritical regime, the critical I regime, the critical II regime, and the supercritical regime, which are analogous to the one-dimensional direct initiation of detonation, are distinguished by varying the dimensionless source energy. However, the typical energy required by each ignition regime is higher than that in the one-dimensional case due to multi-dimensional energy transmission and instabilities. Moreover, the dimensionless source energy should be moderate to obtain a stable free ODW flow field because extremely low source energy leads to ignition failure, while extremely high source energy causes premature ignition. When the inflow Mach number varies, it is found that free ODWs can adjust automatically to a nearly Chapman–Jouguet state, indicating the self-sustaining nature of free detonation waves. Due to this feature, ODWE performance will be relatively stable despite the change in inflow Mach numbers if free ODWs are utilized in the combustor.

© 2021 Author(s). All article content, except where otherwise noted, is licensed under a Creative Commons Attribution (CC BY) license (<http://creativecommons.org/licenses/by/4.0/>). <https://doi.org/10.1063/5.0073035>

I. INTRODUCTION

Oblique detonation waves (ODWs) induced by wedge configurations have been studied extensively in the last few decades because of their potential applications in hypersonic propulsion systems working at extremely high Mach numbers.^{1–3} In these configurations, combustible inflow gases are compressed by the oblique shock wave attached to a wedge, leading to a significant temperature increase and subsequent ignition. If the ignition delay time of post-shock gases is sufficiently short, the combustion wave will couple with the leading oblique shock wave to form an oblique detonation wave instead of shock-induced combustion.⁴ Theoretically,

the initiation and stabilization of ODWs require a certain range of inflow conditions and wedge parameters, which was known as the standing window of oblique detonation.⁵ To meet this requirement, the wedge angle could neither be too small nor too large; otherwise, the ODWs will fail to initiate or detach from the wedge. In practice, the standing behavior of ODWs is also affected by some more realistic factors, such as the boundary layer,⁶ chemical kinetics,⁷ wedge length,⁸ geometric confinement,⁹ and unsteady or non-uniform inflow conditions.^{10,11} The complex effects of these factors over ODWs have been widely studied in recent years to verify the utility of oblique detonation wave engines (ODWEs) under non-ideal conditions.

For typical fuels, the temperature of detonation products could reach 2000–3000 K,^{12–16} which presents a great challenge to the thermal protection system because a practical ODWE is always expected to run continuously for dozens of minutes at a hypersonic speed. According to a recent shock tunnel test,¹⁷ the maximum wall heat flux over the wedge in the combustor of the ODWE is more than 2 MW/m². It can be estimated that the 10-cm-thick stainless steel wall employed in the prototype will fail after running for about 2.5 min and melt after about 5 min without active thermal protection. This formidable problem may be more severe during real flight because the wedge thickness may be reduced to decrease the weight of aircraft, resulting in a more rapid wall temperature increase than that in the shock tunnel test. Moreover, previous studies concerning the ignition of ODWs found that the ignition length decreases with the increase in the wedge angle.³ To ensure successful ignition in a wide range of inflow parameters, the wedge angle is always designed to be large enough to induce an over-driven ODW in most cases.⁶ However, compared with a typical Chapman–Jouguet (C–J) ODW, an over-driven ODW leads only to little benefit in combustion efficiency but larger total pressure loss⁸ and hence larger wave drag. The presence of the wedge wall also causes additional, inevitable skin-friction drag. Therefore, the utilization of the long wedge wall in the combustor of the ODWE has drawbacks from the perspective of both thermal protection and thrust performance.

To cope with significant total pressure loss induced by long wedges, it is suggested to use blunt bodies instead of long, sharp wedges as flame holders in the combustor.^{18–20} In hypersonic inflow of combustible gases, a blunt body induces a normal detonation wave in front of the stagnation point, which develops into an over-driven ODW and finally near the C–J ODW in the downstream.¹⁸ To realize good thrust performance, the size of the blunt body should be relatively small compared to the cross section of the combustor so that the majority of the wave system is in the near C–J state, resulting in low total pressure loss in average. However, tremendous heat flux on the surface of blunt bodies, especially around the stagnation point, poses a great challenge for thermal protection. The harsh thermal environment of hypersonic aircraft engines restricts the utility of blunt bodies as flame holders. In addition, the temperature increase across the normal shock wave is supposed to be sufficiently high to guarantee successful initiation of detonation in a wide range of inflow conditions. In other words, the energy deposition of the blunt body should be larger than the minimum ignition energy of detonation. For a certain configuration, the energy deposition is determined by the size and shape of the blunt body, which is unchangeable during flight. At low Mach numbers, large size and bluntness are favorable to ensure the ignition of detonation, whereas small size and bluntness are preferred at high Mach numbers to reduce the over-driven degree of ODWs. One has to make compromise when designing flame holder parameters to obtain the best overall performance of the ODWE combustor. In comparison, methods to produce non-intrusive, adjustable flame holders instead of wedges, blunt bodies, or other types of wall compression could avoid problems of thermal protection while maintaining good thrust performance, which are meaningful to be explored.

Theoretically, ODWs in configurations where no wedge or other boundary blocks the main flow are referred to as free ODWs.²¹ By a coordinate transformation to a frame attached to the ODW, the normal component of inflow velocity is supposed to be exactly equal

to C–J detonation velocity to guarantee that the free ODW is stable and self-sustained. The early studies concerning the stability of free ODWs ignored their ignition process, which is quite puzzling until Fendell *et al.*²² and Carrier *et al.*²³ suggested that the focusing of a high energy laser beam may be capable of initiating a conical ODW in high-speed flow of combustible gases.^{22,23} Based on laser ignition, a novel combustor configuration was proposed, and the thrust performance of the combustor was analyzed in ideal conditions. However, the concepts of both free ODWs and laser-induced conical detonation waves remain to be theories in the literature. To date, no experimental or even numerical verifications, to the authors' knowledge, have been conducted to develop these ideas into practical applications. In fact, research studies on ODWEs are still in the infancy even though great progress has been made on the initiation and stability of wedge-induced ODWs in recent years. Investigations on alternative ignition methods of ODWs will be helpful in further development of ODWEs.

In the numerical simulations of free ODWs ignited by laser beams, it is extremely difficult to simulate the interaction of the laser and combustible gases satisfactorily because the laser ignition process involves multiple physical effects, such as light absorption, heat conduction, plasma formation, and radiation.^{24,25} The mechanisms of these effects are still under investigations. Phuoc classified the laser ignition of reactive mixtures into four categories: laser thermal ignition, laser-induced photochemical ignition, laser-induced resonant breakdown ignition, and laser-induced spark ignition.²⁶ Among these categories, the laser-induced spark ignition, which relies on high-temperature and high-pressure spark to ignite combustible mixtures, is appropriate to be used in engines.^{27,28} Compared with passive flame holders, such as wedges and blunt bodies, laser sparks act as active flame holders, that is, the energy deposition can be adjusted easily by controlling the output power of laser devices. As a result, the ODWE based on laser spark ignition could run in a relatively stable state and maintain good thrust performance under a variety of sets of inflow conditions. For simplicity, a high-temperature and high-pressure zone was always set as an initial condition to simulate the effect of laser ignition in most studies (for example, Ref. 29), which is also adopted in the present work.

In this paper, numerical simulations based on two-dimensional Euler equations and one-step chemical model are conducted to verify the feasibility of igniting free ODWs by a laser beam in an open space. The formation and flow field structure of free ODWs are analyzed to characterize their thermodynamic and gas-dynamic states. Furthermore, more cases are calculated and compared to investigate the effects of dimensionless source energy and inflow Mach number on the free ODW structure.

II. NUMERICAL METHOD

A simple schematic of the numerical setup to simulate free ODWs ignited by laser spark in high-speed combustible inflow is shown in Fig. 1. The computational domain lies in an open space (without wall constraints) containing a square high-temperature and high-pressure zone, which is modeled as a laser spark. It is noteworthy that in order to achieve detonation initiation, high-energy laser devices that operate in periodically pulsed mode are always used, and the choice of laser pulse frequency is dependent on the coupling between the energy transition process and the detonation dynamics,

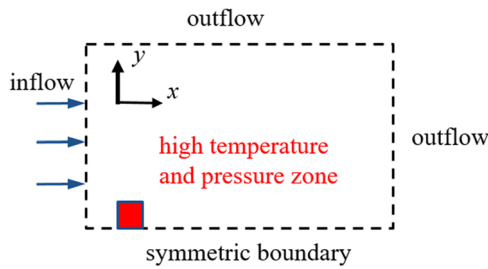


FIG. 1. Schematic of the numerical setup.

which, however, is quite complicated and out of the main focuses of this study. Therefore, by assuming a high-frequency laser spark, the effects of the inputting laser energy are modeled by assigning a persistent high-pressure and high-temperature condition to the spark region at each time step during simulations. Furthermore, high-speed uniformly premixed combustible gases with a Mach number ranging from 10 to 15 enter the computational domain from the left boundary. The upper and right boundaries are set as supersonic outlets. In addition, the lower boundary is set as a symmetric boundary to reduce computational cost.

To simulate the inviscid structure of free ODWs, two-dimensional reactive Euler equations are adopted as governing equations whose non-dimensional form is as follows:

$$\frac{\partial \mathbf{U}}{\partial t} + \frac{\partial \mathbf{F}}{\partial x} + \frac{\partial \mathbf{G}}{\partial y} = \mathbf{S}, \quad (1)$$

where \mathbf{U} , \mathbf{F} , \mathbf{G} , and \mathbf{S} are the vectors of conservative variables, convective fluxes in the x -direction, convective fluxes in the y -direction, and reactive source terms, respectively. They have the following explicit forms:

$$\mathbf{U} = \begin{pmatrix} \rho \\ \rho u \\ \rho v \\ E \\ \rho Z \end{pmatrix}, \quad \mathbf{F} = \begin{pmatrix} \rho u \\ \rho u^2 + p \\ \rho uv \\ (E + p)u \\ \rho uZ \end{pmatrix}, \quad \mathbf{G} = \begin{pmatrix} \rho v \\ \rho uv \\ \rho v^2 + p \\ (E + p)v \\ \rho vZ \end{pmatrix}, \quad \mathbf{S} = \begin{pmatrix} 0 \\ 0 \\ 0 \\ 0 \\ -\dot{\omega} \end{pmatrix}. \quad (2)$$

The variables ρ , u , v , and p are the density, velocity component in the x -direction, velocity component in the y -direction, and pressure, respectively. Z represents the progress variable of chemical reaction, and it varies between 0 and 1. $Z = 0$ denotes the unreacted gases, while $Z = 1$ represents the fully burned gases. E is the total energy per unit volume, which contains internal energy, kinetic energy, and local chemical energy release per unit volume,

$$E = \frac{p}{\gamma - 1} + \frac{\rho(u^2 + v^2)}{2} + \rho(1 - Z)Q, \quad (3)$$

where Q is the total chemical energy per unit mass and γ is the specific heat ratio. $\dot{\omega}$ is the chemical reaction rate, which is modeled by one-step Arrhenius kinetics in this study,

$$\dot{\omega} = -k\rho(1 - Z)\exp\left(-\frac{E_a}{T}\right), \quad (4)$$

where k and E_a are the rate constant and activation energy, respectively. It should be noted that due to the absence of crossover temperature,³⁰ one-step chemistry has some limitations in simulating real detonation dynamics governed by chain-branching kinetics. However, it had been demonstrated to be capable of reproducing various phenomena observed in experiments qualitatively.³¹ Moreover, as compared to detailed chemistry and multi-step simplified models, it has many other advantages, such as the simple formula, low computational cost, and absence of arbitrary parameters.³² Therefore, one-step chemistry has been widely employed in many fundamental studies of detonation physics,^{33–35} and it is also adopted in this paper to study the fundamental characteristics of free ODWs. The above equations are solved using the ideal thermal equation of state as follows:

$$p = \rho T. \quad (5)$$

All these variables are non-dimensionalized by reference to the values in the unreacted state,

$$\begin{aligned} \rho &= \frac{\tilde{\rho}}{\tilde{\rho}_0}, \quad p = \frac{\tilde{p}}{\tilde{p}_0}, \quad T = \frac{\tilde{T}}{\tilde{T}_0}, \quad u = \frac{\tilde{u}}{\sqrt{\tilde{R}\tilde{T}_0}}, \quad v = \frac{\tilde{v}}{\sqrt{\tilde{R}\tilde{T}_0}}, \\ x &= \frac{\tilde{x}}{\tilde{L}_{1/2}}, \quad y = \frac{\tilde{y}}{\tilde{L}_{1/2}}, \quad E_a = \frac{\tilde{E}_a}{\tilde{R}\tilde{T}_0}, \quad Q = \frac{\tilde{Q}}{\tilde{R}\tilde{T}_0}, \\ t &= \frac{\tilde{t}}{\tilde{L}_{1/2}/\sqrt{\tilde{R}\tilde{T}_0}}, \quad k = \frac{\tilde{k}}{\sqrt{\tilde{R}\tilde{T}_0}/\tilde{L}_{1/2}}, \end{aligned} \quad (6)$$

where the superscript \sim represents dimensional variables and subscript 0 denotes the parameters of the unburned mixture. Note that coordinate variables x and y are scaled by the half reaction zone length $\tilde{L}_{1/2}$ to present the grid resolution across the detonation wave conveniently, which was first introduced by Erpenbeck³⁶ and was widely used as a reference length scale in dimensionless studies of detonation.^{21,33–35} In this way, the rate constant k is calculated when the values of other parameters are given. The gas constant R of reactants and products is assumed to be the same so that it can be eliminated in the nondimensionalized process of the ideal thermal equation of state, as shown in Eq. (5). The dimensionless variables in the one-step chemical model are fixed at $Q = 50$, $\gamma = 1.2$, $E_a = 15$, and $k = 7.6648$ to simulate the free ODW structures induced by a laser spark. Notably, this parameter set of the

TABLE I. Numerical cases conducted in this paper.

Case no.	Inflow Mach number Ma	Dimensionless source energy E_s	Ignition regime
1	12	1 500	Critical II
2	12	500	Subcritical
3	12	800	Critical I
4	12	10 000	Supercritical
5	10	1 500	Critical II
6	11	1 500	Critical II
7	13	1 500	Critical II
8	14	1 500	Critical II
9	15	1 500	Critical II

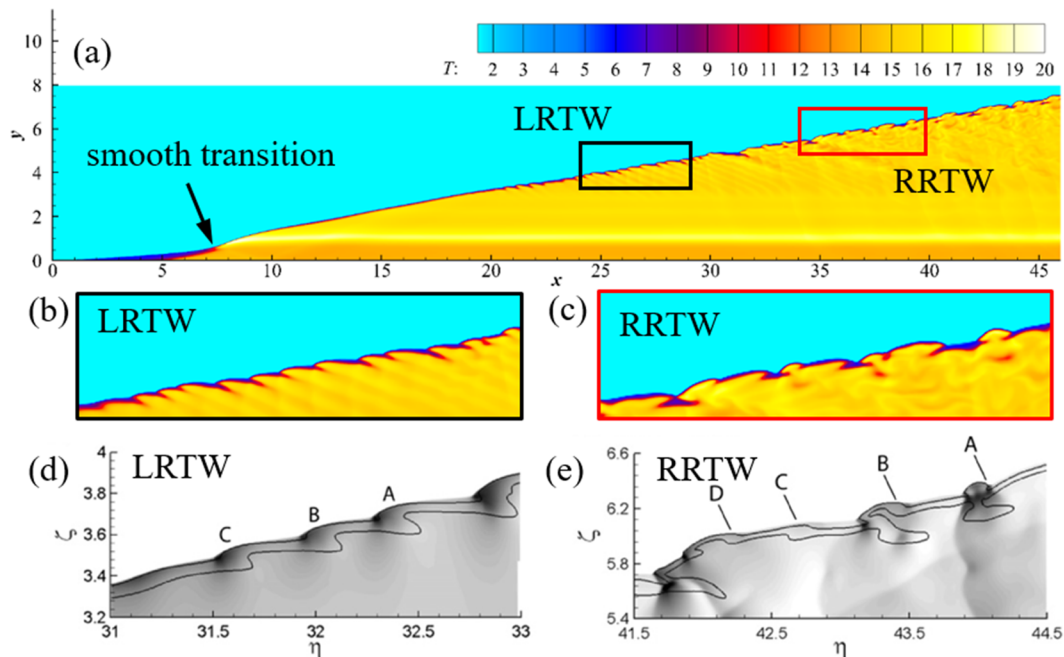


FIG. 2. Oblique detonation cellular structures ($\theta = 24^\circ$, $Q = 50$, $\gamma = 1.2$, $E_a = 50$, and $Ma = 15$): (a) overall temperature contours, (b) local enlarged view of the LRTW, (c) local enlarged view of the RRTW, and (d) LRTW and (e) RRTW calculated by Verreault *et al.*⁴⁴

one-step chemical model does not correspond to a specific combustible mixture, but it had been widely used in many fundamental studies of ODWs.^{33,35,37} In the laser spark, gases are initially at rest. Following the previous study,³¹ the dimensionless source energy E_s , rather than the source temperature or source pressure, is selected as the control parameter to discuss various ignition regimes. According to Eq. (3), the dimensionless source energy can be expressed as $E_s = p_s/(\gamma - 1)$. Notably, the dimensionless density in the spark region is almost unchanged due to the rapid energy deposition process, and it is equal to 1 approximately. Hence, the corresponding temperature and pressure inside the spark region can be calculated as follows: $T_s = p_s = (\gamma - 1) E_s$. Simulations are carried out by varying the inflow Mach number from 10 to 15 and the dimensionless source energy from 150 to 10 000. Various initiation phenomena can be observed. Nine typical cases of them are chosen and discussed in this paper to explore the effects of the inflow Mach number and source energy on the initiation characteristics of free ODWs, as summarized in Table I.

An in-house code based on the finite difference method is employed to solve the above governing equations in discrete form. The dispersion-controlled dissipative (DCD) scheme³⁸ and three-order Runge–Kutta method are adopted in the spatial discretion and time marching in numerical calculation, respectively. Detailed descriptions and validations of the computation code in shock waves and detonation problems can be found in the previous studies.^{3,39–43} In this paper, a new verification case of the ODW cellular structure is conducted to further validate the feasibility of the code in ODW dynamics, as shown in Fig. 2. The numerical setup is the same as that of Verreault *et al.*⁴⁴ (wedge angle $\theta = 24^\circ$, $Q = 50$, $\gamma = 1.2$, $E_a = 50$, and $Ma = 15$). In Fig. 2(a), a smooth transition from the oblique shock

wave to the ODW, the left-running transverse wave (LRTW), and right-running transverse wave (RRTW) can be distinguished. The flow patterns of the LRTW and RRTW are consistent with those calculated in the literature.⁴⁴ It can be concluded that the present code is capable of simulating wave interactions and transient structures of ODWs.

The size of the computational domain shown in Fig. 1 is 200×100 , which corresponds to 8×10^6 Cartesian grids in total when the grid resolution is 20 points per half reaction length. Since an explicit time-marching method is employed, the time step should be subject to the Courant–Friedrichs–Lewy (CFL) condition. In this study, the CFL number is set as 0.4 in all cases, resulting in a dimensionless time step on the order of 10^{-4} . The coordinate origin is set at the lower left corner, and the x -axis is parallel to the direction of inflow. The side length of the square laser spark, whose center locates at (5.5, 0.5), is set as unity.

III. RESULTS AND DISCUSSION

A. Initiation and structure of free ODWs

In this section, the flow field structure and its temporal evolution in case 1 are presented to show the fundamental characteristics of free ODWs initiated by non-intrusive energy deposition. The inflow Mach number and dimensionless source energy of case 1 are 12 and 1500, respectively, which are moderate among all numerical cases. Figure 3 shows the pressure distribution at several typical instants during the flow field evolution. In the early stage ($t = 2.43$), an initial blast wave is triggered by the tremendous pressure difference between the laser spark zone and main flow, which travels downstream under the influence of high-speed inflow. Subsequently,

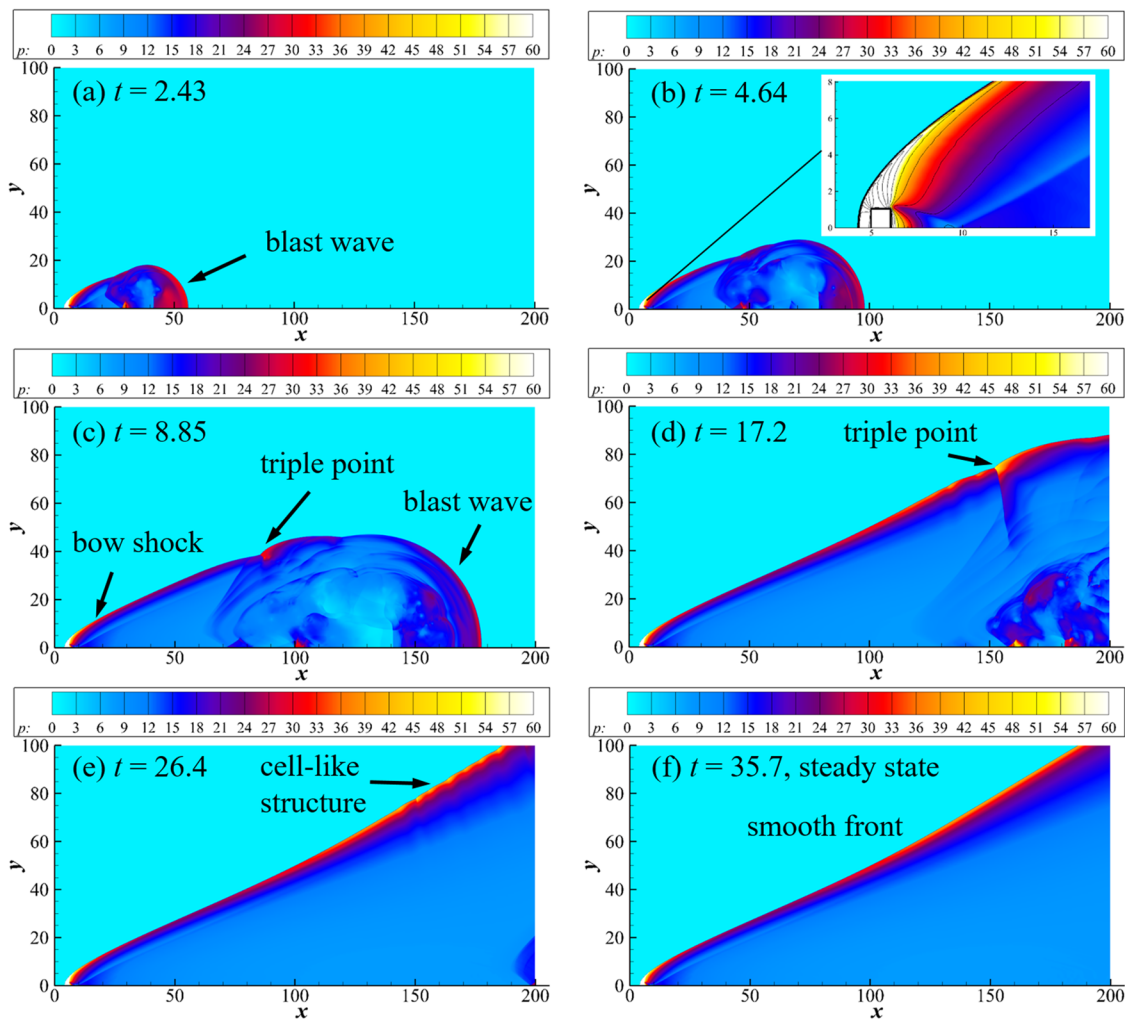


FIG. 3. Temporal evolution of pressure contours in case 1: (a) $t = 2.43$, (b) $t = 4.64$, (c) $t = 8.85$, (d) $t = 17.2$, (e) $t = 26.4$, and (f) $t = 35.7$.

a normal shock wave appears ahead of the spark and develops into a bow shock in the downstream [see the local enlarged view in Fig. 3(b)], which is similar to the ODW structure around a blunt body in supersonic flow.^{18–20} Although the inflow around $y = 0$ is strongly blocked by high-pressure laser spark, no stagnation point is observed in the flow field, which is different from the flow characteristic around blunt bodies. At $t = 8.85$, it can be clearly seen that the interaction between the initially formed blast wave and bow shock leads to a triple point as shown in Fig. 3(c). With time going by, the triple point moves downstream together with the initial blast wave. At $t = 17.2$, the majority of the initial blast wave has been blown out of the computational domain. At $t = 26.4$, it is observed that more triple points split off the main triple point, exhibiting an unstable cell-like structure near the upper outlet. At $t = 35.7$, all triple points have traveled out of the upper boundary, leaving a smooth wave front in the computational domain. The flow fields shown in Fig. 3(f) are steady since the structure remains unchanged from $t = 35.7$ to $t > 100$. Figure 4 further shows the temporal evolution of

temperature distribution at typical instants corresponding to Fig. 3, except for Fig. 4(e). The cell-like structure seems to be more clear at $t = 28.7$ in the temperature flow field. The reaction zone is represented by the region enclosed by the two isolines of $Z = 0.05$ and $Z = 0.95$ in Fig. 4(f). It is observed that the shape change of the reaction zone is consistent with that of the shock front, indicating the strong coupling between the shock and flame. Since no wedge or other wall conditions block the main flow, the wave system shown in Figs. 3(f) and 4(f) is indeed of free ODW structures described in the literature.²¹

Figure 5 shows the peak pressure distribution at several chosen instants. The pressure data are extracted from lines parallel to the x -axis and compared to find the maximum one as peak pressure at a certain y value. The peak pressure profile indicates the distribution of shock strength along the y -axis since the post-shock pressure is typically much higher than other parts of the flow field. Tremendous peak pressure is observed near $y = 0$ due to the strong compression effect of the normal shock wave. As y increases, the normal shock

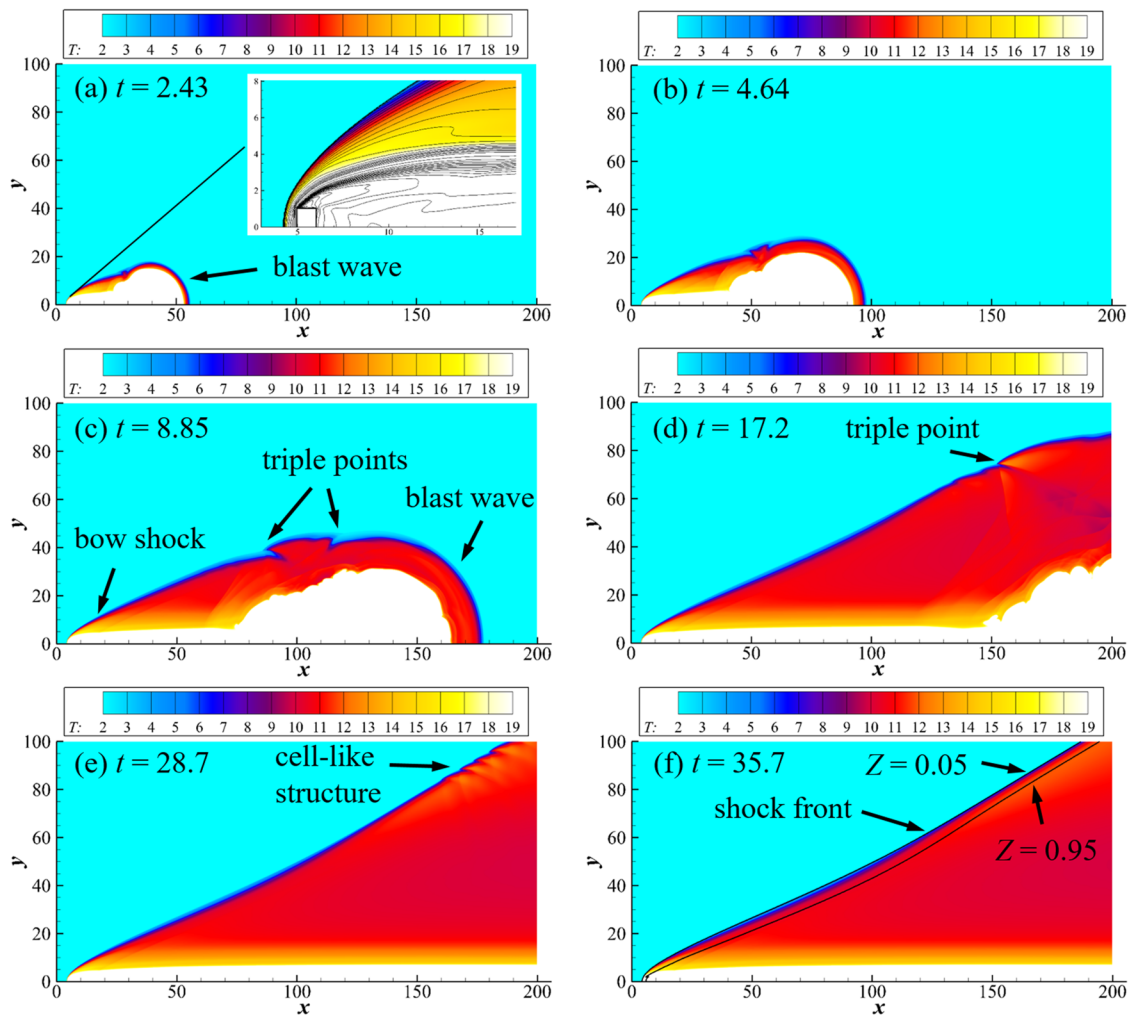


FIG. 4. Temporal evolution of temperature contours in case 1: (a) $t = 2.43$, (b) $t = 4.64$, (c) $t = 8.85$, (d) $t = 17.2$, (e) $t = 28.7$, and (f) $t = 35.7$.

develops into a bow shock whose strength decreases continuously. Finally, the shock strength increases to a constant value after a transition process, which corresponds to the formation of oblique shock waves with a certain shock angle. At $t = 8.85$, the sudden jump of peak pressure around $y = 40$ implies the emergence of the triple point shown in Figs. 3(c) and 4(c). The triple point splits into several ones between $t = 17.2$ and $t = 26.4$. At $t = 35.7$, the peak pressure after $y = 75$ gets close to 41.89, the theoretical von-Neumann pressure in the C-J state, indicating that the free ODW formed in the downstream is a C-J ODW that can be self-sustained. Before the C-J ODW part, however, the peak pressure undergoes a period of decrease from very high values caused by normal shock to a minimum value of 25.63 around $y = 29$ and then increases to a stable value of 41.89. Similar trends of shock angles can also be found in Figs. 3(f) and 4(f), which implies an under-driven transition zone between the bow shock and C-J ODW. In fact, this transition zone structure also appears in other cases (case 5–9) at inflow Mach numbers $Ma = 10$ –15, among which the transition process is particularly

obvious at low Mach numbers. The phenomenon will be further analyzed in Secs. III B and C.

A mesh refinement test over case 1 is conducted to guarantee that the above discussions are based on sufficient grid resolution. Figure 6(a) shows the flow field simulated with grid sizes of 20 points per half reaction length (pts/ $\bar{L}_{1/2}$, upper) and 40 points per half reaction length (lower). The position of the normal shock wave, the evolution process from the bow shock to oblique shock, the temperature contour, and the pressure isolines are very close between upper and lower results. Only tiny difference can be detected by careful comparison, indicating that the present grid resolution (20 pts/ $\bar{L}_{1/2}$) is sufficient in revealing the flow field structure of free ODWs. In Fig. 6(b), shock angle distributions at various grid sizes are further compared quantitatively. It is essential to obtain shock angle distributions accurately in the present work because several ignition regimes will be distinguished based on the characteristics of the shock angle profile in Sec. III B. When very rough grids are adopted (2 pts/ $\bar{L}_{1/2}$), the measured shock angle curve shows slight oscillation.

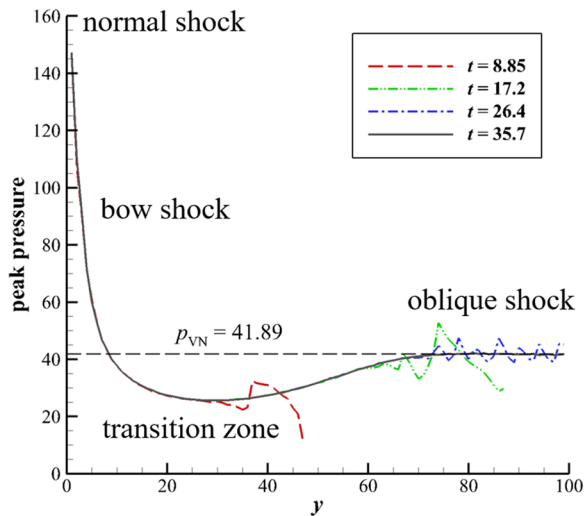


FIG. 5. Temporal evolution of peak pressure distributions in case 1.

Meanwhile, the transition zone structure is not revealed according to shock angle distribution, which is unacceptable. With mesh refinement, the oscillation disappears and the transition zone becomes more and more clear. The shock angle of the oblique shock wave can be well captured with every grid resolution shown in Fig. 6(b), which implies that the simulation of the bow shock and transition zone structure primarily requires fine grids. The features of shock angle distribution can be well captured in simulations with the grid resolution of 10 pts/ $\tilde{L}_{1/2}$, 20 pts/ $\tilde{L}_{1/2}$, and 40 pts/ $\tilde{L}_{1/2}$. It can be concluded

that a grid resolution of over 20 points per half reaction length is fine enough to simulate the free ODW flow field by the present numerical method and is employed in this study. Notably, because a constant CFL number (i.e., 0.4) is adopted in this study, the increase in grid resolution also results in an increasing resolution in time integration. Hence, the appropriateness of the time step is also verified in the above grid resolution tests.

B. Effects of dimensionless source energy

The above numerical results of case 1 indicate that ODWs, which fit the features of free ODWs described in the literature,²¹ can be initiated by non-intrusive energy deposition under appropriate circumstances. In Sec. III A, the laser spark configuration and inflow parameters are fixed, that is, 1×1 square laser spark, source energy $E_s = p_s/(\gamma - 1) = 1500$, spark temperature $T_s = 300$, and inflow Mach number $Ma = 12$. Apparently, the ignition behavior is dependent on these parameters so that different combinations of them may result in distinctive structures of the free ODW flow field. The effects of dimensionless source energy and inflow Mach number are analyzed in this section and Sec. III C, respectively, to promote the understanding of free ODWs induced by non-intrusive methods.

To reveal the influence of dimensionless source energy, extensive cases are conducted numerically with E_s ranging from 150 to 10000 while keeping other parameters unchanged. Both the corresponding spark temperature T_s and spark pressure p_s range from 30 to 2000. Based on these data, four ignition regimes are classified, the typical E_s values of which are 500 (subcritical regime, case 2), 800 (critical I regime, case 3), 1500 (critical II regime, case 1), and 10000 (supercritical regime, case 4), respectively. Figure 7 shows

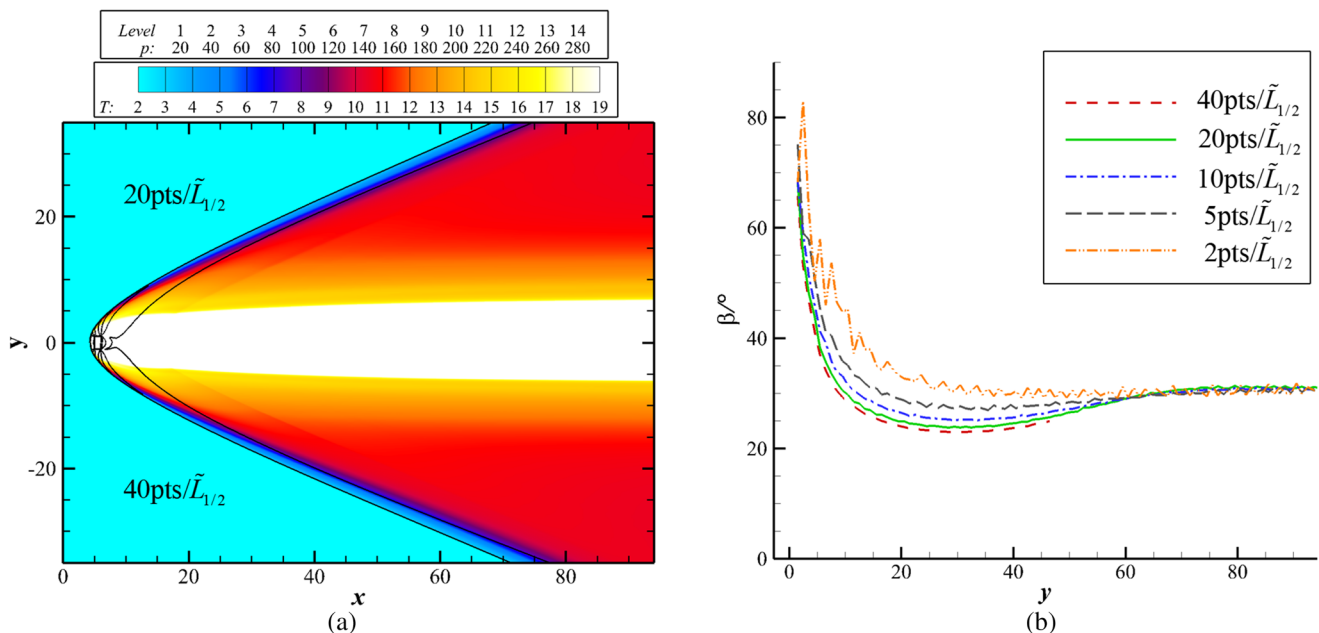


FIG. 6. Mesh refinement test over case 1: (a) pressure and temperature contours at the grid resolution of the present study (20 points per half reaction length) and finer grids (40 points per half reaction length) and (b) shock angle distribution at different grid resolutions.

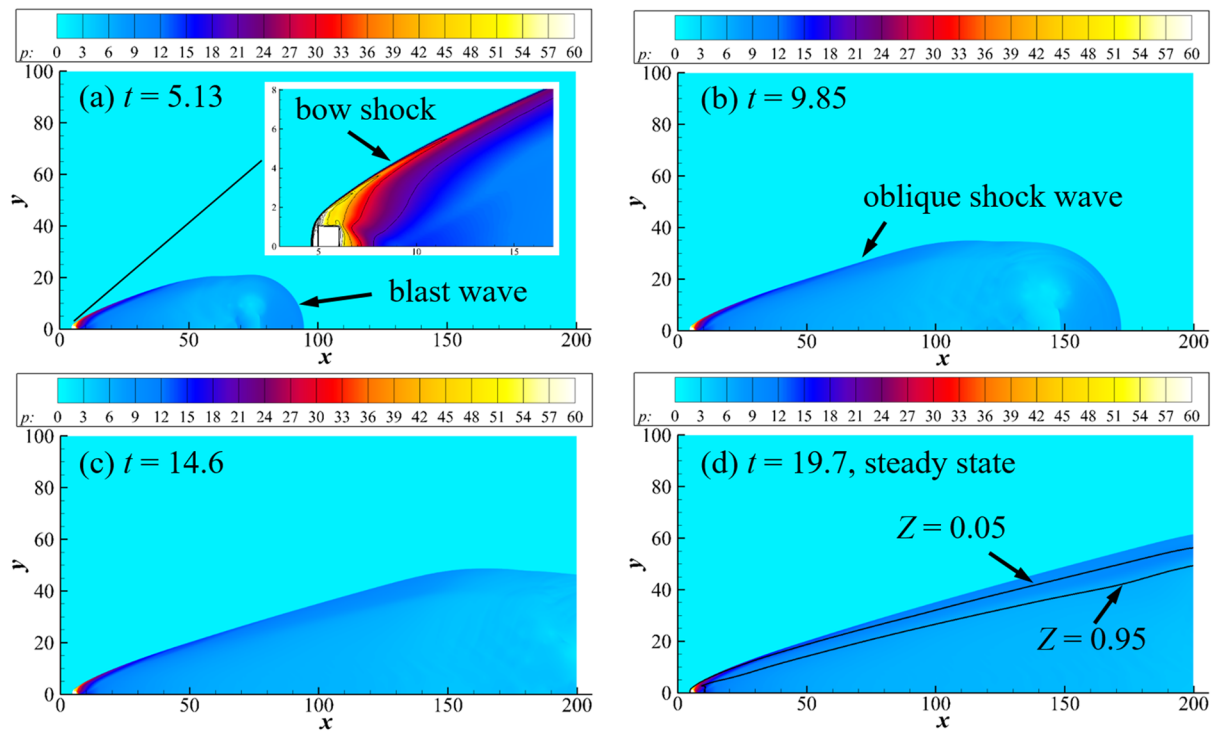


FIG. 7. Temporal evolution of pressure contours in case 2: (a) $t = 5.13$, (b) $t = 9.85$, (c) $t = 14.6$, and (d) $t = 19.7$.

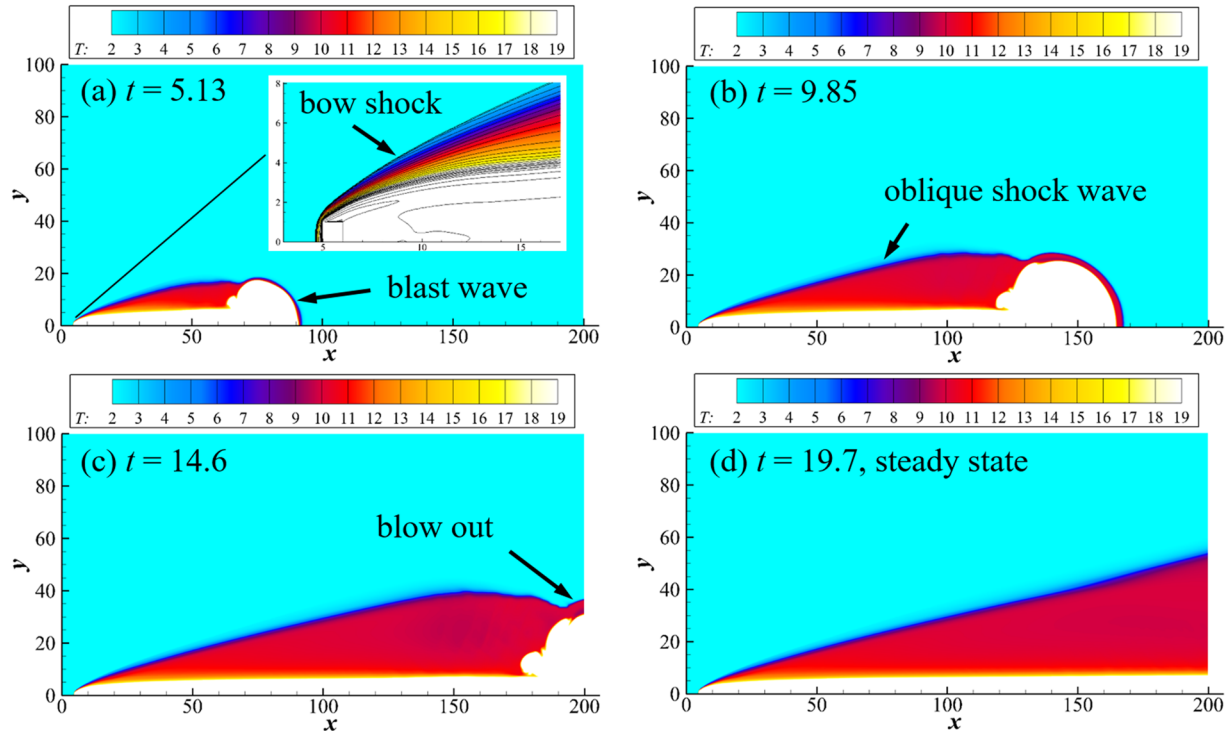


FIG. 8. Temporal evolution of temperature contours in case 2: (a) $t = 5.13$, (b) $t = 9.85$, (c) $t = 14.6$, and (d) $t = 19.7$.

the temporal evolution of the pressure field in case 2. Note that the contour levels of Fig. 7 are the same as those of Fig. 3. The comparison between Figs. 7(a) and 3(b) shows a similar flow field structure shortly after calculation starts, which contains an initial blast wave traveling downstream, a bow shock, and a normal shock upstream of laser spark. However, the pressure jump across the blast wave and post-wave pressure gradient are less significant in case 2. According to the local enlarged view around laser spark in Fig. 7(a), the standoff distance of the normal shock wave is smaller than that in Fig. 3(b). The above differences can be attributed to the lower strength of the initial blast wave resulted from weaker laser spark in case 2. At $t = 9.85$, the post-shock pressure drops rapidly when the bow shock converts to the oblique shock wave. At $t = 14.6$, the initial blast wave has been blown out of the computational domain. At $t = 19.7$, an inert oblique shock wave, whose shock angle is much

smaller than that of the ODW shown in Fig. 3(f) and still decreases, remains in the steady solution of the flow field. It is also found that the reaction zone, which is represented by the region between $Z = 0.05$ and $Z = 0.95$, decouples with the shock front after about $x = 40$, indicating the initiation failure of free ODWs. The above features are further illustrated in the temperature field of Fig. 8. The contour levels in Fig. 8 are the same as those of Fig. 4. Compared with Figs. 4(d) and 4(e), the initial blast wave in case 2 is so weak that no significant triple point is observed before a steady state is reached, which may be crucial for the formation of the transition zone and the initiation of ODWs. As a result, the ignition fails in this regime.

As the dimensionless source energy increases to 800 in case 3, the free ODW is initiated successfully, but the ignition regime is distinct with that in case 1. Between $t = 3.87$ and $t = 10.9$, the flow field

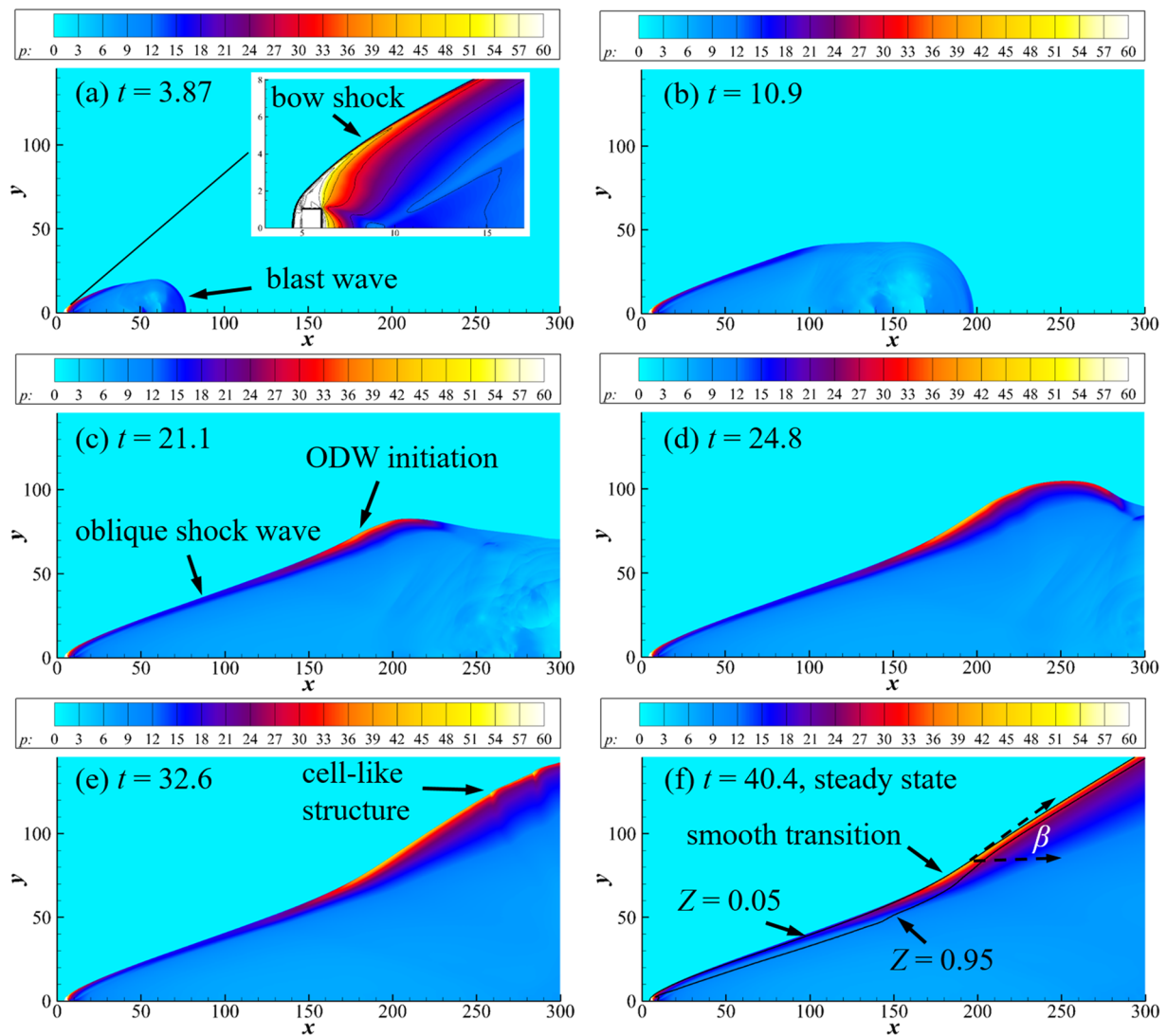


FIG. 9. Temporal evolution of pressure contours in case 3: (a) $t = 3.87$, (b) $t = 10.9$, (c) $t = 21.1$, (d) $t = 24.8$, (e) $t = 32.6$, and (f) $t = 40.4$.

structure is closer to case 2 since the initial blast wave is very weak. At $t = 21.1$, however, the oblique shock wave is enhanced by the compression waves generated by post-shock combustion, resulting in the local initiation of ODWs. At $t = 24.8$, it is observed that the shock angle increases in the downstream of local initiation. Similar to Fig. 3(e), the perturbation caused by ODW initiation evolves into cell-like structures at $t = 32.6$. Then, the cell-like structures travel out of the computational domain and the flow field is steady after $t = 40.4$. The spatial evolution of the reaction zone is more complex than case 1 and case 3. In the downstream of laser spark, it is found that the reaction zone thickness grows larger and larger, which implies a continuous decrease in the reaction rate. Although the coupling between the shock front and flame seems to be weaker, a gradually growing compression wave catches up with the shock front

around $x = 190$, subsequently leading to the initiation of ODWs. The ignition structure shown in Fig. 9 is similar to the smooth transition of ODWs over wedges.⁴⁵ This ignition regime is distinguished from case 1 mainly due to the existence of the ignition structure. The local shock angle during the ignition is larger than that of the ODW angle in the downstream, as is shown in Fig. 9(f). In fact, the ignition produces a slightly over-driven ODW, which then decays into the C-J state. This feature will be discussed in detail later. Note that the initiation of free ODWs in case 2 requires a relatively long distance due to small E_s so that the computational domain is specially enlarged to show the wave structure completely. The temporal evolution of the temperature flow field is further illustrated in Fig. 10.

As E_s increases from 800 to 1500, the ODW ignition position moves upstream and the over-driven degree after ignition decreases

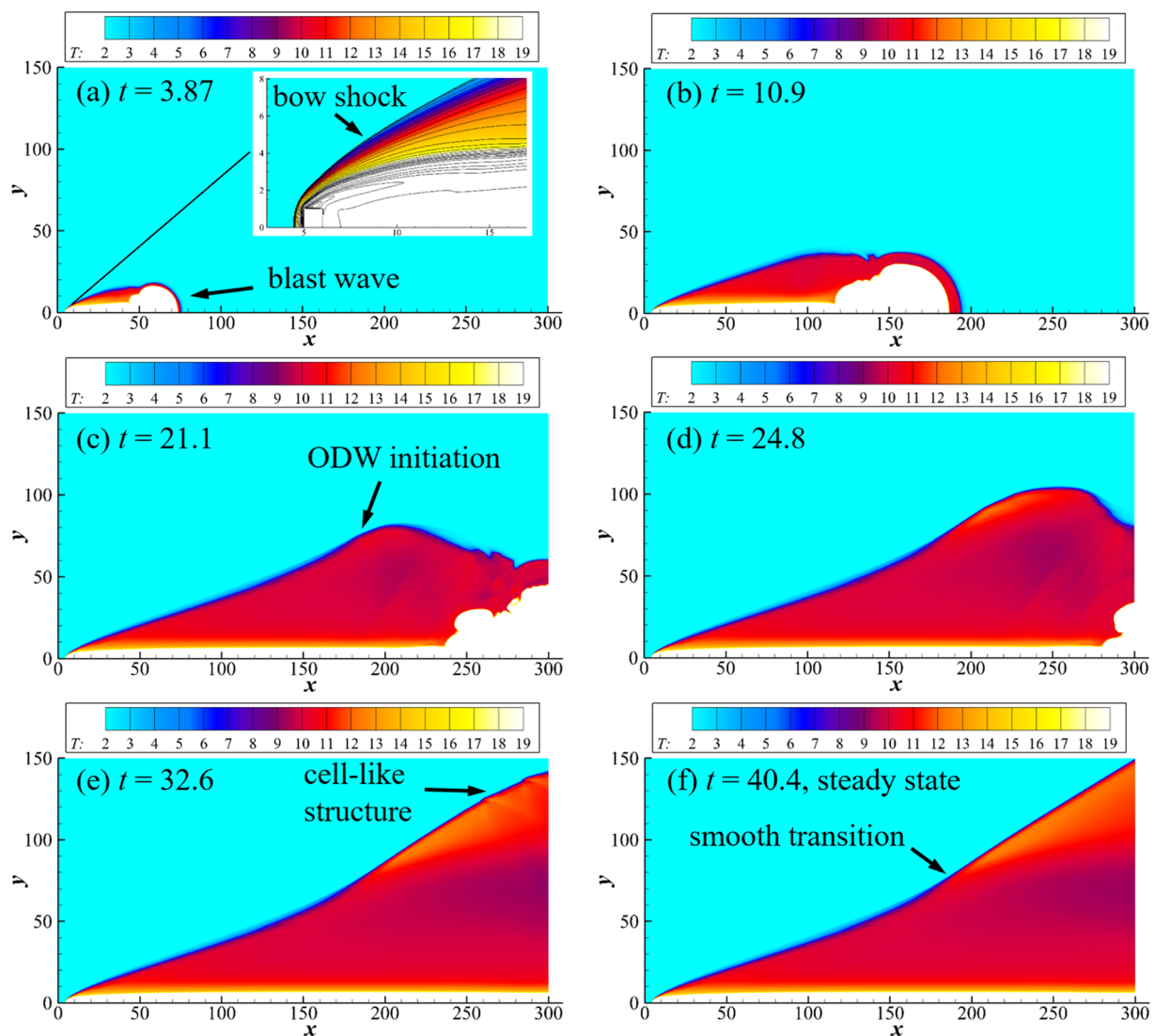


FIG. 10. Temporal evolution of temperature contours in case 3: (a) $t = 3.87$, (b) $t = 10.9$, (c) $t = 21.1$, (d) $t = 24.8$, (e) $t = 32.6$, and (f) $t = 40.4$.

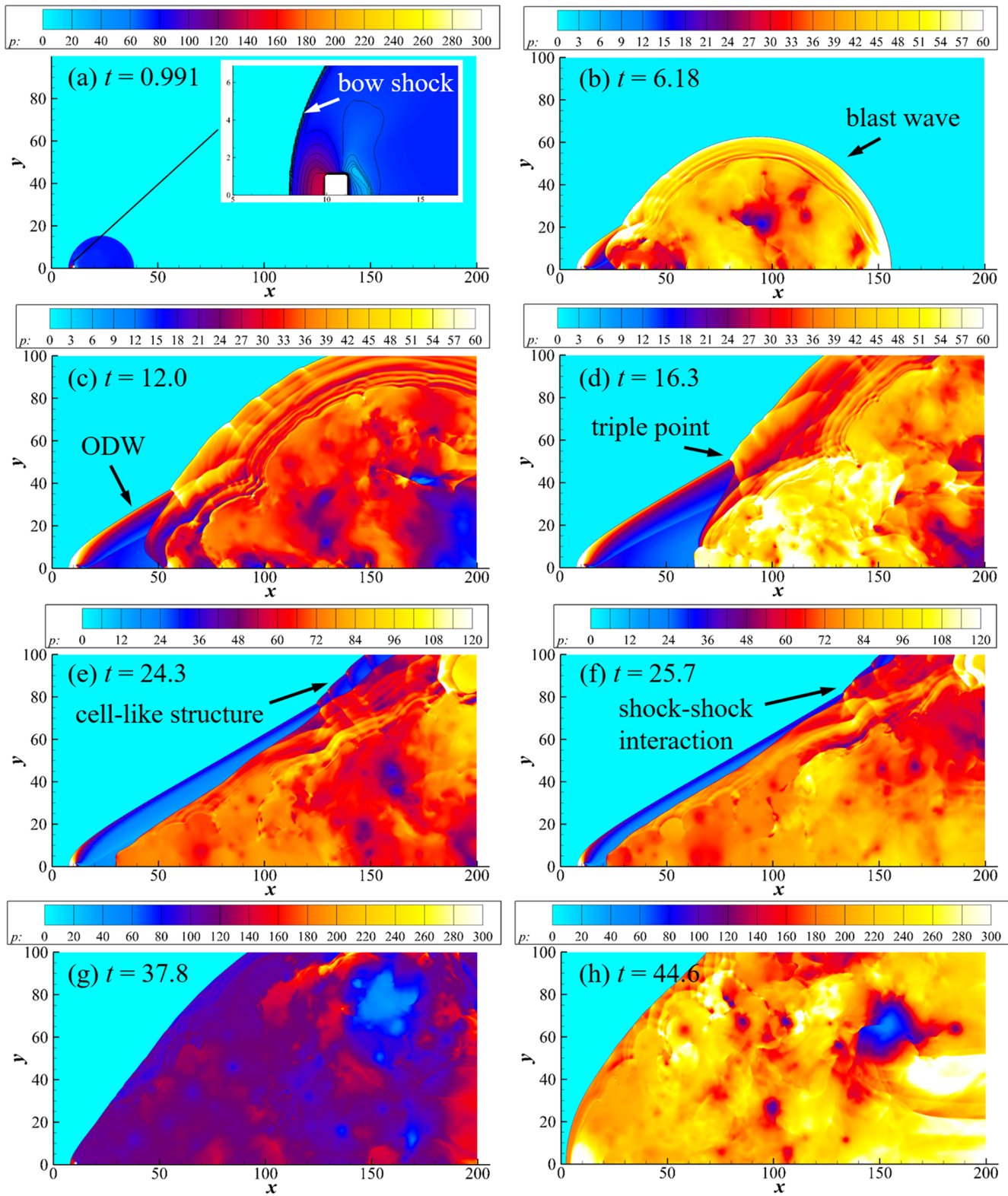


FIG. 11. Temporal evolution of pressure contours in case 5: (a) $t = 0.991$, (b) $t = 6.18$, (c) $t = 12.0$, (d) $t = 16.3$, (e) $t = 24.3$, (f) $t = 25.7$, (g) $t = 37.8$, and (h) $t = 44.6$.

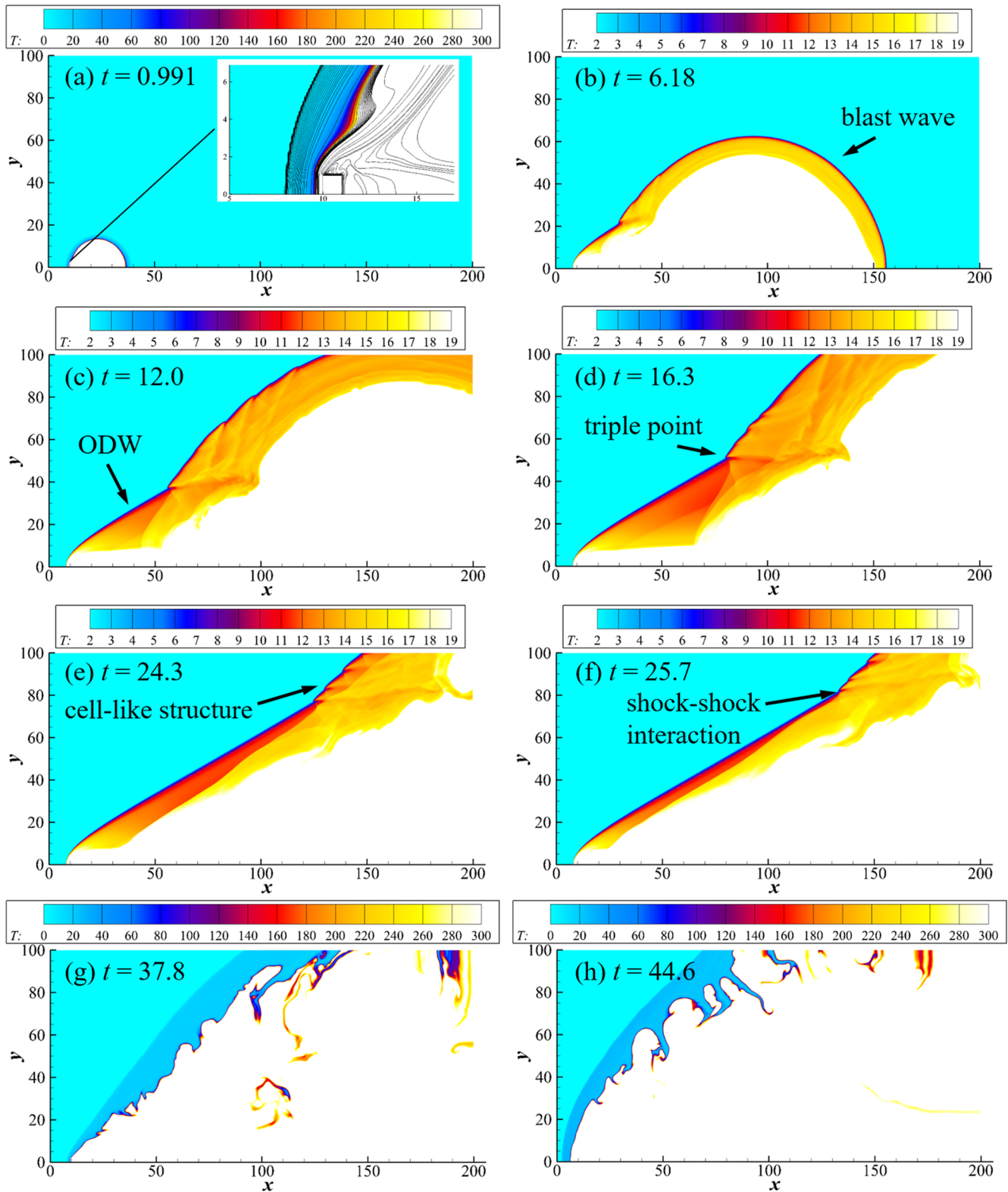


FIG. 12. Temporal evolution of temperature contours in case 5: (a) $t = 0.991$, (b) $t = 6.18$, (c) $t = 12.0$, (d) $t = 16.3$, (e) $t = 24.3$, (f) $t = 25.7$, (g) $t = 37.8$, and (h) $t = 44.6$.

to unity, which is shown in Figs. 3 and 4. The variation of the over-driven degree along the ODW front can be interpreted by the distribution of the detonation angle. With a further increase in E_s , the transition zone structure becomes less obvious. That is, the transition between the bow shock and oblique shock wave happens more rapidly. Meanwhile, the peak pressure does not decrease much during the transition when higher E_s is adopted. Similar trends are also observed by varying E_s from 1500 up to about 10 000. However, E_s cannot be increased all the time; otherwise, the stable ODW structure will be destructed. In case 4, dimensionless source energy takes a very high value of $E_s = 10\,000$. The pressure flow fields at 8 typical instants in case 4 are shown in Fig. 11. At $t = 0.991$, a very strong blast wave has been triggered by the tremendous pressure gradient between laser spark and main flow, which travels faster than that in any other cases presented in this work. Between $t = 6.18$ and $t = 16.3$, the temporal evolution of the shock front is similar to that in case 1, while a significant non-uniform distribution of pressure and instabilities are observed in post-shock gases. At $t = 24.3$, the main triple point also splits into several triple points, which exhibits a cell-like structure. The compression waves generated by chemical reaction are so strong that they evolve into a shock wave, which has approached the shock front. Note that the contour levels are adjusted to reveal the flow field details after Fig. 11(e). At $t = 25.7$, shock-shock interaction is observed, which results in a stronger shock wave propagating upstream. At $t = 37.8$, the wave structure of free ODWs has been totally erased. At $t = 44.6$, the shock front approaches the left boundary, which indicates premature ignition that affects the running state of combustors. The temperature flow field at the typical instants described above is shown in Fig. 12.

It can be concluded from the above analysis that the ignition regime is greatly influenced by changing the dimensionless source energy E_s . Specifically, four ignition regimes can be classified in cases 1–4, among which free ODWs are obtained in case 1 and case 3. To initiate and maintain a stable free ODW structure, E_s should be neither too small nor too large. Insufficient source energy leads to ignition failure (case 2), while excessive source energy results in premature ignition (case 4), both of which should be avoided in propulsion systems. The four ignition regimes presented above are analogous to the one-dimensional direct initiation of detonation waves. Figure 13(a) shows the shock velocity evolution of four typical one-dimensional cases with different source energies. One-dimensional numerical simulations are conducted over a tube with the left end closed and the right end opened. A unit-length ignition zone, which is consistent with two-dimensional simulations, is placed at the left end. The same numerical algorithms are adopted, together with the same grid resolution of $20 \text{ pts}/\bar{L}_{1/2}$.

In Fig. 13(a), the initiation energy is too low to induce a detonation wave at $E_s = 250$. The shock velocity of the blast wave resulting from high-temperature and high-pressure spark decreases gradually when it travels to the right. At $E_s = 400$, the initial blast wave does not result in a detonation wave either. However, a local hotspot emerges at around $x = 80$, which enhances the intensity of chemical reaction together with shock strength to initiate a detonation wave. The detonation wave is over-driven after initiation and then decays to the C–J state, in which the detonation velocity is a constant. At $E_s = 625$, the shock velocity decreases below C–J detonation velocity and then increases to initiate a detonation wave, which never

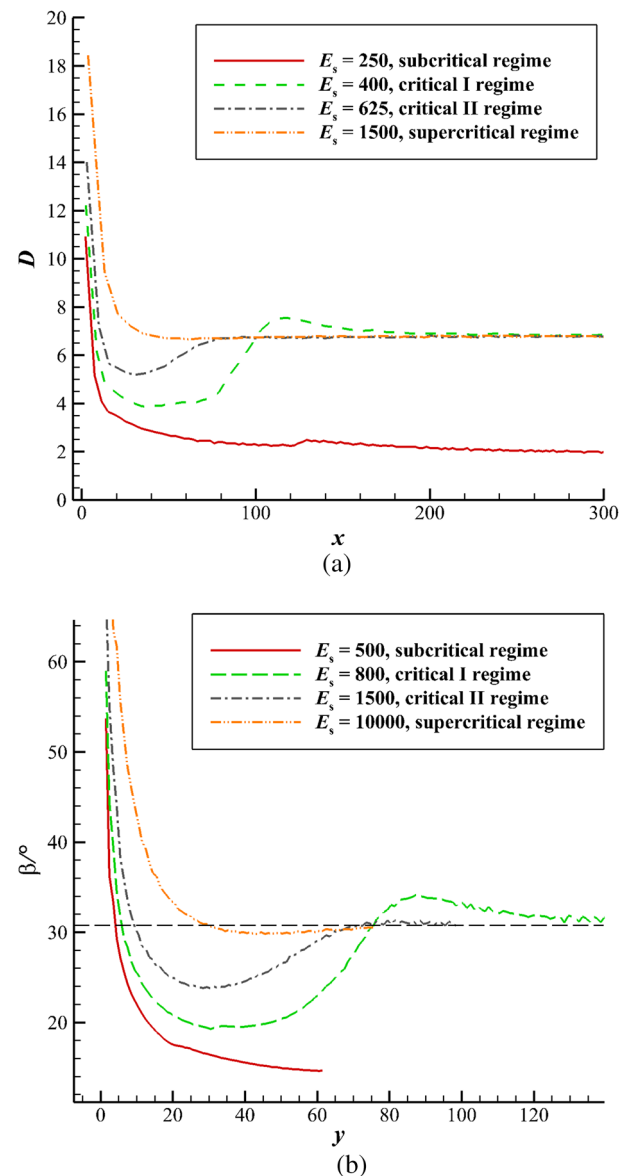


FIG. 13. Four initiation modes of (a) one-dimensional detonation and (b) free ODWs when the dimensionless source energy E_s varies. D and β stand for the leading shock velocity in one-dimensional cases and oblique shock angle in two-dimensional simulation, respectively.

undergoes any over-driven period. At $E_s = 1500$, the strong energy source manages to initiate a detonation wave directly. The shock velocity is higher than the C–J detonation velocity during the whole process. According to previous numerical and experimental research studies,^{31,46} ignition regimes are referred to as subcritical initiation and supercritical initiation in cases where $E_s = 250$ and $E_s = 1500$. When $E_s = 400$ and 625 , both regimes are classified as the critical initiation regime. In this study, they are further distinguished as critical I regime and critical II regime according to whether the detonation wave is over-driven or not after ignition.

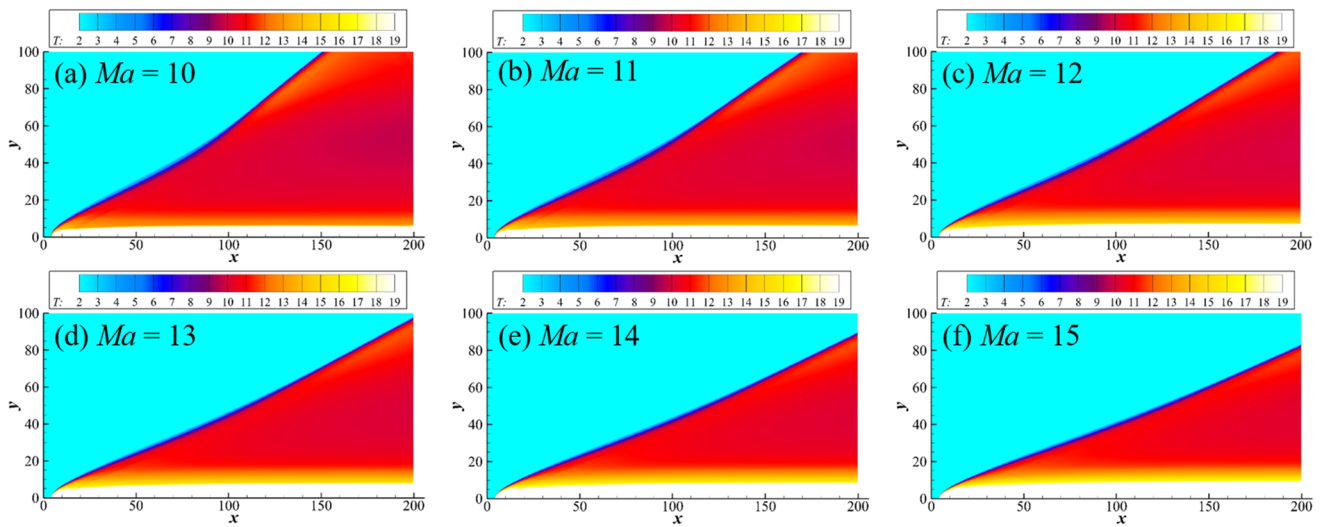


FIG. 14. Temperature contour of the oblique detonation flow field at different inflow Mach numbers: (a) $Ma = 10$ (case 1), (b) $Ma = 11$ (case 5), (c) $Ma = 12$ (case 6), (d) $Ma = 13$ (case 7), (e) $Ma = 14$ (case 8), and (f) $Ma = 15$ (case 9).

To compare with one-dimensional cases, the shock angle distributions are given in Fig. 13(b). Note that the shock angle distribution in case 4 is collected at $t = 25.7$ before the free ODW front is erased. As illustrated by Eq. (7), the sinusoidal of the shock angle β equals the inflow velocity component normal to the shock front v_{0n} divided by inflow velocity v_0 . In the coordinate frame fixed to the shock front, v_{0n} is exactly the shock velocity D in the frame where unreacted gases are at rest. When the inflow velocity v_0 is a constant, the trend of the β profile is comparable to the D profile in the one-dimensional case. By comparing Fig. 13(a) with Fig. 13(b), it is found that the four ignition regimes of free ODWs show the same characteristics as one-dimensional direct initiation of detonation. The results indicate a close relationship between free ODWs and one-dimensional, self-sustaining detonation, which was predicted by Stewart and Kasimov.²¹ At $E_s = 500$, detonation initiation fails in the two-dimensional case but occurs successfully in one-dimensional simulation. Moreover, the typical dimensionless source energies required for each ignition regime in the two-dimensional case are larger than those in the one-dimensional case. On one hand, the energy transmission is less concentrated in two-dimensional cases. For example, the characteristic waves traveling in the positive direction of the x -axis converge into the initial blast wave, which barely contributes to the formation of ODWs. In other words, the effective energy that supports detonation initiation in the two-dimensional case is smaller than that in the one-dimensional condition. On the other hand, free ODWs undergo two-dimensional instabilities, which is more complex and requires more extra energy than one-dimensional detonation propagation. Consequently, the four ignition regimes of free ODWs are analogous to the one-dimensional direct ignition of detonation waves, but the corresponding source energies are higher,

$$\sin \beta = \frac{v_{0n}}{v_0} = \frac{Ma_n}{Ma}. \quad (7)$$

C. Effects of the inflow Mach number

The influence of the inflow Mach number on the free ODW structure is further explored in this section. Figure 14 shows the steady temperature flow fields at $Ma = 10$ – 15 (cases 1 and 5–9). In these cases, E_s is kept at 1500. The ignition behavior of free ODWs in the six cases presented in Fig. 14 all belongs to the critical II regime. Transition zones, within which the shock angle and shock strength are lower, can be distinguished between the bow shock and oblique shock. It is found that the transition zone structure

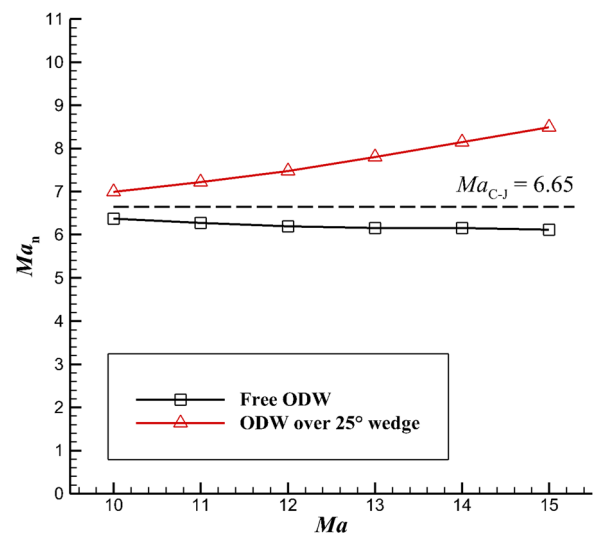


FIG. 15. Variation of the Mach number component perpendicular to the wave surface Ma_n with the inflow Mach number of free oblique detonation waves and standing oblique detonation waves over a 25° wedge.

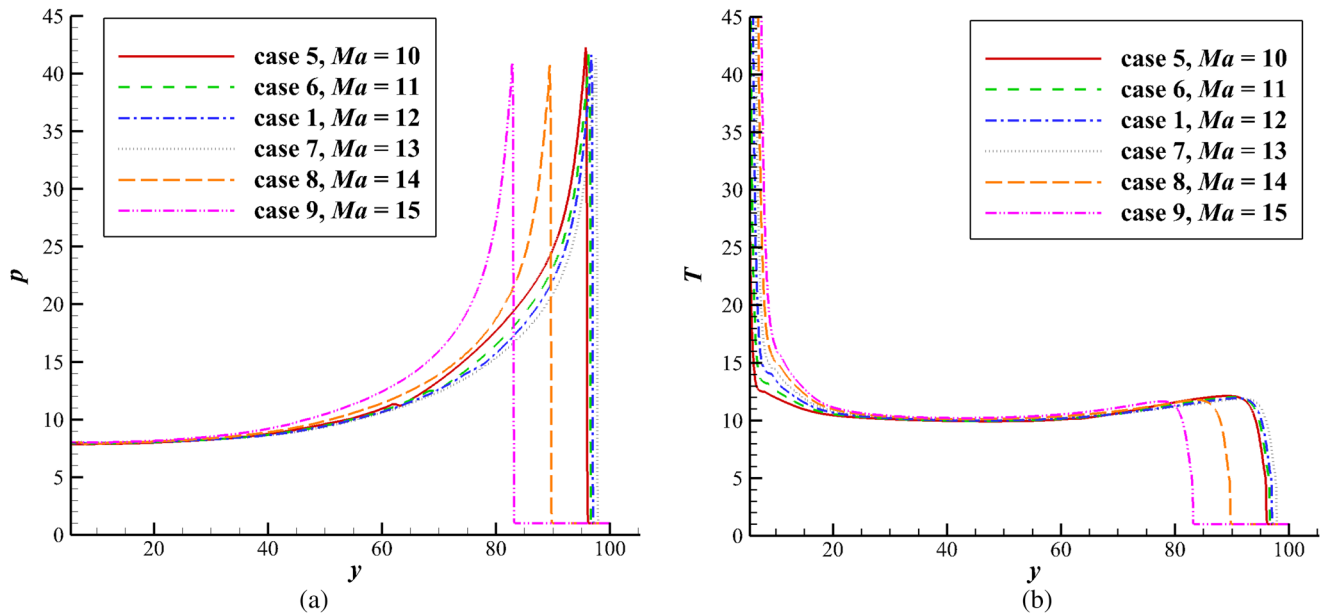


FIG. 16. Pressure (a) and temperature (b) distributions at the outlet of the computational domain.

becomes less conspicuous with the increase in the inflow Mach number. Moreover, the detonation angle downstream of the transition zone decreases slightly when the inflow Mach number increases. Theoretically, Ma_n equals the shock Mach number in the C-J state, which remains unchanged when the inflow Mach number varies. According to Eq. (7), $\sin\beta$ becomes smaller with the increase in Ma , eventually resulting in the decrease in the detonation angle β ,

$$D_{C-J} = \sqrt{\frac{(\gamma^2 - 1)Q}{2}} + \sqrt{c_0^2 + \frac{(\gamma^2 - 1)Q}{2}} \approx \sqrt{2(\gamma^2 - 1)Q}. \quad (8)$$

To verify that Ma_n does not change with Ma as indicated by theory and illustrate this favorable feature of free ODWs in application, Fig. 15 shows the variation of Ma_n over Ma in the numerical results. For free ODWs induced by laser spark, the calculated Ma_n value is slightly below the theoretical C-J value (6.65) calculated using Eq. (8). The discrepancy may attribute to chemical kinetics that are not considered in theory. In Fig. 4(f), for example, the reaction zone thickness is negligible compared to the length scale of the computational domain, whereas it is assumed to be infinitesimal in classical C-J theory. The effective energy release of combustion that supports the ODW front may be smaller than total heat release Q due to the complexity of the two-dimensional heat release process. Consequently, the inflow velocity component normal to the shock front is smaller than the one-dimensional theoretical C-J value according to Eq. (8) so that Ma_n is less than Ma_{C-J} as the inflow sonic speed is constant. It is also found that the Ma_n value of free ODWs remains almost unchanged with the increase in Ma . However, for typical ODWs over a certain wedge (for example, 25° wedge), the values of Ma_n rise together with Ma . ODWs over the 25° wedge are always over-driven, whose Ma_n is larger than the theoretical C-J value and that of free ODWs. The results are similar when other wedge angles

are chosen, as long as they lie on the over-driven regime of the detonation polar diagram.⁵ The comparison implies that the thermodynamic state of free ODWs is stable under the variation of the inflow Mach number, which results from the self-sustaining nature of free detonation waves. To further illustrate this feature of free ODWs, pressure and temperature distributions at the outlet of the computational domain are plotted in Fig. 16. For cases 1, 5, and 6, the outlet is chosen just before the ODWs reach the upper boundary to show the pressure and temperature jump across the detonation wave. For cases 7–9, the outlet is simply the right boundary of the computational domain. Although the positions of detonation waves are different due to the changes in the inflow Mach number, all curves collapse together in the middle of the outlet. In other words, the same detonation wave strength is achieved with the variation of the inflow Mach number. This feature makes free ODWs favorable in practical applications of ODWEs because the detonation angle can adjust automatically to adapt to changing inflow Mach numbers, keeping the combustion in a relatively stable state, i.e., the near C-J state.

IV. CONCLUSION

In this paper, a series of numerical simulations of free ODWs induced by a laser spark are conducted based on the non-dimensional Euler equations and one-step chemical model. Three conclusions drawn through the analysis presented above are as follows:

- (1) In an open space, energy deposition caused by the non-intrusive method is capable of initiating a free ODW under appropriate conditions.
- (2) When source energy is varied, four initiation regimes of free ODWs are distinguished, namely, the subcritical regime,

the critical I regime, the critical II regime, and the supercritical regime. The ignition regimes are analogous to the one-dimensional direct initiation of detonation. However, the dimensionless source energy required by each regime is higher than the corresponding one-dimensional case due to the multi-dimensional energy transmission and instabilities. To obtain a stable free ODW flow field, the dimensionless source energy should be neither too high nor too low; otherwise, initiation failure or premature ignition may occur.

- (3) As the inflow Mach number changes, the detonation angle of free ODWs adjusts automatically to keep the post-shock pressure and temperature in the C–J state, which is referred to as the self-adaption feature of free ODWs. This feature is favorable in applying free ODWs to ODWEs because the engine could run in a relatively steady state at varying inflow Mach numbers.

ACKNOWLEDGMENTS

This work was supported by the National Natural Science Foundation of China (Grant Nos. 11672312 and 11532014).

AUTHOR DECLARATIONS

Conflict of Interest

The authors have no conflicts to disclose.

DATE AVAILABILITY

The data that support the findings of this study are available from the corresponding author upon reasonable request.

REFERENCES

- ¹D. A. Rosato, M. Thornton, J. Sosa, C. Bachman, G. B. Goodwin, and K. A. Ahmed, "Stabilized detonation for hypersonic propulsion," *Proc. Natl. Acad. Sci. U. S. A.* **118**, e2102244118 (2021).
- ²G. X. Xiang, X. Gao, W. J. Tang, X. Z. Jie, and X. Huang, "Numerical study on transition structures of oblique detonations with expansion wave from finite-length cowl," *Phys. Fluids* **32**, 056108 (2020).
- ³H. Teng, H. D. Ng, and Z. Jiang, "Initiation characteristics of wedge-induced oblique detonation waves in a stoichiometric hydrogen-air mixture," *Proc. Combust. Inst.* **36**, 2735 (2017).
- ⁴C. Li, K. Kailasanath, and E. S. Oran, "Detonation structures behind oblique shocks," *Phys. Fluids* **6**, 1600 (1994).
- ⁵D. T. Pratt, J. W. Humphrey, and D. E. Glenn, "Morphology of standing oblique detonation waves," *J. Propul. Power* **7**, 837 (1991).
- ⁶Z. Zhang, C. Wen, W. Zhang, Y. Liu, and Z. Jiang, "Formation of stabilized oblique detonation waves in a combustor," *Combust. Flame* **223**, 423 (2021).
- ⁷Z. Xu, G. Dong, Z. Pan, and M. Gui, "Standing window of oblique detonation with pathological behaviour," *Chin. J. Aeronaut.* **34**, 496 (2021).
- ⁸G. Xiang, X. Li, X. Sun, and X. Chen, "Investigations on oblique detonations induced by a finite wedge in high altitude," *Aerosp. Sci. Technol.* **95**, 105451 (2019).
- ⁹K. L. Wang, Z. J. Zhang, P. F. Yang, and H. H. Teng, "Numerical study on reflection of an oblique detonation wave on an outward turning wall," *Phys. Fluids* **32**, 046101 (2020).
- ¹⁰P. Yang, H. D. Ng, and H. Teng, "Numerical study of wedge-induced oblique detonations in unsteady flow," *J. Fluid Mech.* **876**, 264 (2019).
- ¹¹K. Iwata, S. Nakaya, and M. Tsue, "Wedge-stabilized oblique detonation in an inhomogeneous hydrogen-air mixture," *Proc. Combust. Inst.* **36**, 2761 (2017).
- ¹²W. Han, W. Liang, C. Wang, J. X. Wen, and C. K. Law, "Spontaneous initiation and development of hydrogen-oxygen detonation with ozone sensitization," *Proc. Combust. Inst.* **38**, 3575 (2021).
- ¹³G. Emanuel and D. Tuckness, "Steady, oblique, detonation waves," *Shock Waves* **13**, 445 (2004).
- ¹⁴G. Xiang, H. Li, R. Cao, and X. Chen, "Study of the features of oblique detonation induced by a finite wedge in hydrogen-air mixtures with varying equivalence ratios," *Fuel* **264**, 116854 (2020).
- ¹⁵G. Xiang, Y. Zhang, X. Gao, H. Li, and X. Huang, "Oblique detonation waves induced by two symmetrical wedges in hydrogen-air mixtures," *Fuel* **295**, 120615 (2021).
- ¹⁶Q. Meng, N. Zhao, and H. Zhang, "On the distributions of fuel droplets and *in situ* vapor in rotating detonation combustion with prevaporized *n*-heptane sprays," *Phys. Fluids* **33**, 043307 (2021).
- ¹⁷Z. L. Jiang, Z. J. Zhang, Y. F. Liu, C. Wang, and C. T. Luo, "Criteria for hypersonic airbreathing propulsion and its experimental verification," *Chin. J. Aeronaut.* **34**, 94 (2020).
- ¹⁸P. R. Ess, J. P. Sislian, and C. B. Allen, "Blunt-body generated detonation in viscous hypersonic ducted flows," *J. Propul. Power* **21**, 667 (2005).
- ¹⁹I. A. Bedarev, V. M. Temerbekov, and A. V. Fedorov, "Simulating the regimes of oblique detonation waves arising at detonation initiation by a small-diameter projectile," *Thermophys. Aeromechanics* **26**, 59 (2019).
- ²⁰Y. Fang, Z. Zhang, Z. Hu, and X. Deng, "Initiation of oblique detonation waves induced by a blunt wedge in stoichiometric hydrogen-air mixtures," *Aerosp. Sci. Technol.* **92**, 676 (2019).
- ²¹D. S. Stewart and A. R. Kasimov, "State of detonation stability theory and its application to propulsion," *J. Propul. Power* **22**, 1230 (2006).
- ²²F. Fendell, J. Mitchell, R. McGregor, and M. Sheffield, "Laser-initiated conical detonation wave for supersonic combustion. II," *J. Propul. Power* **9**, 182 (1993).
- ²³G. F. Carrier, F. E. Fendell, and S. F. Fink, "Nonintrusive stabilization of a conical detonation wave for supersonic combustion," *Combust. Flame* **103**, 281 (1995).
- ²⁴J. F. MacArt, J. M. Wang, P. P. Popov, and J. B. Freund, "Detailed simulation of laser-induced ignition, spherical-flame acceleration, and the origins of hydrodynamic instability," *Proc. Combust. Inst.* **38**, 2341 (2021).
- ²⁵P. Patane and M. Nandgaonkar, "Review: Multipoint laser ignition system and its applications to IC engines," *Opt. Laser Technol.* **130**, 106305 (2020).
- ²⁶T. X. Phuoc, "Laser-induced spark ignition fundamental and applications," *Opt. Laser Technol.* **44**, 351 (2006).
- ²⁷B. An, Z. Wang, L. Yang, X. Li, and C. Liu, "The ignition characteristics of the close dual-point laser ignition in a cavity based scramjet combustor," *Exp. Therm. Fluid Sci.* **101**, 136 (2019).
- ²⁸B. An, L. Yang, Z. Wang, X. Li, M. Sun, J. Zhu, and W. Yan, "Characteristics of laser ignition and spark discharge ignition in a cavity-based supersonic combustor," *Combust. Flame* **212**, 177 (2020).
- ²⁹M. H. Morsy and S. H. Chung, "Numerical simulation of front lobe formation in laser-induced spark ignition of CH₄-air mixtures," *Proc. Combust. Inst.* **29**, 1613 (2002).
- ³⁰Y. Wang, W. Han, R. Deiterding, and Z. Chen, "Effects of disturbance on detonation initiation in H₂/O₂/N₂ mixture," *Phys. Rev. E* **3**, 123201 (2018).
- ³¹J. H. S. Lee and A. J. Higgins, "Comments on criteria for direct initiation of detonation," *Philos. Trans. R. Soc. London, Ser. A* **357**, 3503 (1999).
- ³²H. Teng, H. D. Ng, P. Yang, and K. Wang, "Near-field relaxation subsequent to the onset of oblique detonations with a two-step kinetic model," *Phys. Fluids* **33**, 096106 (2021).
- ³³W. Han, Y. Gao, C. Wang, and C. K. Law, "Coupled pulsating and cellular structure in the propagation of globally planar detonations in free space," *Phys. Fluids* **27**, 106101 (2015).
- ³⁴Y. N. Zhang, L. Zhou, J. S. Gong, H. D. Ng, and H. H. Teng, "Effects of activation energy on the instability of oblique detonation surfaces with a one-step chemistry model," *Phys. Fluids* **30**, 106110 (2018).

- ³⁵K. C. K. Uy, L. Shi, and C.-Y. Wen, "Numerical analysis of the vibration-chemistry coupling effect on one-dimensional detonation stability," *Aerosp. Sci. Technol.* **107**, 106327 (2020).
- ³⁶J. J. Erpenbeck, "Stability of idealized one-reaction detonations," *Phys. Fluids* **7**, 684 (1964).
- ³⁷H. Ng, A. Higgins, C. Kiyanda, M. Radulescu, J. Lee, K. Bates, and N. Nikiforakis, "Nonlinear dynamics and chaos analysis of one-dimensional pulsating detonations," *Combust. Theor. Model.* **9**, 159 (2005).
- ³⁸Z. L. Jiang, "On dispersion-controlled principles for non-oscillatory shock-capturing schemes," *Acta Mech. Sin.* **20**, 1 (2004).
- ³⁹P. Yang, H. Teng, H. D. Ng, and Z. Jiang, "A numerical study on the instability of oblique detonation waves with a two-step induction-reaction kinetic model," *Proc. Combust. Inst.* **37**, 3537 (2019).
- ⁴⁰H. Teng, L. Zhou, P. Yang, and Z. Jiang, "Numerical investigation of wavelet features in rotating detonations with a two-step induction-reaction model," *Int. J. Hydrogen Energy* **45**, 4991 (2020).
- ⁴¹P. Yang, H. Teng, Z. Jiang, and H. D. Ng, "Effects of inflow Mach number on oblique detonation initiation with a two-step induction-reaction kinetic model," *Combust. Flame* **193**, 246 (2018).
- ⁴²Z. Jiang, G. Han, C. Wang, and F. Zhang, "Self-organized generation of transverse waves in diverging cylindrical detonations," *Combust. Flame* **156**, 1653 (2009).
- ⁴³Z. Jiang, L. Chang, and F. Zhang, "Dynamic characteristics of spherically converging detonation waves," *Shock Waves* **16**, 257 (2007).
- ⁴⁴J. Verreault, A. J. Higgins, and R. A. Stowe, "Formation of transverse waves in oblique detonations," *Proc. Combust. Inst.* **34**, 1913 (2013).
- ⁴⁵H. H. Teng and Z. L. Jiang, "On the transition pattern of the oblique detonation structure," *J. Fluid Mech.* **713**, 659 (2012).
- ⁴⁶M. I. Radulescu, A. J. Higgins, S. B. Murray, and J. H. S. Lee, "An experimental investigation of the direct initiation of cylindrical detonations," *J. Fluid Mech.* **480**, 1 (2003).